THE ASTROPHYSICAL JOURNAL, 391:121–136, 1992 May 20

THE KINEMATICS OF THE MOLECULAR GAS IN CENTAURUS A

A. C. QUILLEN,[1] P. T. DE ZEEUW,[2] E. S. PHINNEY,[1] AND T. G. PHILLIPS[3]
California Institute of Technology
Received 1991 March 14; accepted 1991 September 24

ABSTRACT

The CO (2–1) emission along the inner dust lane of Centaurus A, observed with the Caltech Submillimeter Observatory on Mauna Kea, shows the molecular gas to be in a thin disk, with a velocity dispersion of only about 10 km s^{-1}. The observed line profiles are broadened considerably due to beam smearing of the gas velocity field. The profile shapes are inconsistent with planar circular and noncircular motion. However, a warped disk in a prolate potential provides a good fit to the profile shapes. The morphology and kinematics of the molecular gas is similar to that of the ionized material, seen in Hα. The best-fitting warped disk model not only matches the optical appearance of the dust lane but also agrees with the large-scale map of the CO emission and is consistent with H I measurements at larger radii.

Subject headings: galaxies: individual (NGC 5128) — galaxies: kinematics and dynamics — galaxies: ISM — ISM: molecules

1. INTRODUCTION

As the nearest of all the giant radio galaxies, Centaurus A (NGC 5128) provides a unique opportunity to observe in detail the dynamics and morphology of an active galaxy at a variety of different wavelengths. Because of the prominent disk of dust and gas in its central region, Cen A is suspected to be the product of the merging of a small spiral with a larger elliptical galaxy (Baade & Minkowski 1954). Numerical simulations of galaxy collisions (Hernquist & Quinn 1988, 1989) indeed show shell-like features similar to those observed in the outer parts of Cen A (Malin, Quinn, & Graham 1983). By studying the kinematics and morphology of the dust lane, we may hope to learn how the gas in the AGN becomes nonplanar and misaligned from the host galaxy—as it is observed to be in both radio Seyfert galaxies (Unger et al. 1987; Haniff, Wilson, & Ward 1988) and in radio ellipticals galaxies (Sansom et al. 1987), and as it is inferred from the infrared spectra to be in distant quasars (Sanders et al. 1989).

The dust and gas in Cen A have been traced in a variety of different species and wavelengths, including H I (van Gorkom et al. 1990), Hα (Bland, Taylor, & Atherton 1987, hereafter BTA), CO(1–0) emission and far-infrared (Eckart et al. 1990b), CO(2–1) emission (Phillips et al. 1987), near-infrared emission of stars (Harding, Jones, & Rodgers 1981; Giles 1986) and dust (Joy et al. 1988), and also in absorption against the optical light (Dufour et al. 1979), and at millimeter and radio wavelengths (Gardner & Whiteoak 1976; Eckart et al. 1990a; Seaquist & Bell 1990; Israel et al. 1991). Here we present new and more complete measurements of the ^{12}CO(2–1) emission with somewhat higher angular resolution than the CO(1–0) data of Eckart et al. (1990b).

The optical morphology of the warped dust lane has been modeled as a transient by Tubbs (1980) and as an equilibrium structure in a rotating triaxial galaxy by van Albada, Kotanyi, & Schwarzschild (1982). The observed stellar rotation does not support the latter (Wilkinson et al. 1986). Van Gorkom et al. (1990) interpreted the H I 21 cm data by circular motion in a spherical potential. The twisted Hα velocity field of the dust lane (BTA) has been modeled by putting the gas on tilted rings, i.e., the orbits are circles, but the orbital planes have inclination that varies with radius (Nicholson, Bland, & Taylor 1992). This approach is similar to what has long been customary in studies of H I in spiral galaxies (Bosma 1981; Schwarz 1985; Begeman 1987). Asymmetries and twists in the observed velocity field of a galaxy can also be the result of gas on noncircular orbits, such as occur in a triaxial potential. Bertola et al. (1991) have had success modeling the kinematics of the optical emission line gas in NGC 5077 with a triaxial potential, and Lees (1991) has had similar success modeling the H I emission from NGC 4278. In this paper we explore both kinds of models, as have Staveley-Smith et al. (1990) in their recent study of Michigan 160. Specifically, we attempt to interpret our data with three different sets of models: (1) axisymmetric models with gas in a plane on circular orbits, (2) triaxial models with gas in a plane on noncircular orbits, and (3) axisymmetric models with gas on inclined circular orbits.

Hα emission is detectable in the central regions of Cen A with high spatial resolution (BTA). However, the velocity resolution of the Hα data is lower than that of the CO data. We show that the molecular material (CO) and the ionized material (Hα) are dynamically and geometrically identical systems. Since dynamical time scales in the central region are significantly shorter than they are at the larger radii where 21 cm H I is observed, and since the cooling time scale for molecular material is significantly shorter than for ionized material, we expect the molecular gas to be in a more relaxed configuration, i.e., the kinematics should be determined primarily by the potential of the galaxy and not by the initial conditions of the merger. Furthermore, if the galaxy is triaxial, deviations from circular motion generally are expected to be largest in the central regions (de Zeeuw and Franx 1989, hereafter ZF). If the gas were initially in one plane inclined with respect to the principal plane of the galaxy and is now warped as a result of differential precession (Tubbs 1980), the warp should be most severe in the central regions because the differential precession

1 Theoretical Astrophysics, 151–33, California Institute of Technology, Pasadena, CA 91125.
2 Postal address: Sterrewacht, Huygens Laboratorium, Postbus 9513, 2300 RA Leiden, The Netherlands.
3 Downs Laboratory of Physics, 320–47, California Institute of Technology, Pasadena, CA 91125.

rate scales with the rate of change of the angular velocity of the gas, which should be largest at about 1 kpc from the nucleus, where the rotation curve begins to flatten out. As a result, CO provides us with an ideal tracer of the galactic potential and the geometry of the gas in the inner kiloparsec of the galaxy.

In § 2 we present new measurements of the ^{12}CO(2–1) emission along the inner part of the dust lane of Cen A. In § 3 we discuss the thickness of the disk. Our kinematic modeling approach is outlined in § 4, and models with gas on circular orbits in a plane are explored in § 5. In § 6 we relax the assumption of circularity and allow planar elliptic orbits in triaxial potentials. In § 7 we relax the assumption that the gas is in a plane but consider only circular orbits in axisymmetric potentials. We summarize our results in § 8.

2. OBSERVATIONS

Observations of Centaurus A in the $J = 2 \rightarrow 1$ transition of ^{12}CO were made at the Caltech Submillimeter Observatory (CSO) on Mauna Kea in 1989 March and 1991 June. A description of the CSO can be found in Phillips et al. (1987). At a rest frequency of 230 GHz, the beam size is 30″ FWHM. The velocity resolution was 1.3 km s^{-1} over a range of 650 km s^{-1}.

Figure 1 shows the CO(2–1) spectra with a linear baseline removed for 18 positions observed in 1989 March along the dust lane at position angle (PA) $-63°.5$. The central position coincides with the unresolved continuum source in the nucleus of Cen A (van der Hulst, Golisch, & Haschick 1983). The spacing is a half-beam in the inner part of the dust lane and a full beam at the outermost positions. Displayed along with modeled profile shapes in Figures 4*a*, 5*a*, and 8*a* is a mostly filled 11 by 7 grid of positions centered on the nuclear position observed in 1991 June (see Fig. 8*c* for a picture of beam positions). The spacing is a half-beam along PA 26°.5 and a full beam along PA $-63°.5$. The data were calibrated both by the usual ambient/chopper technique, and by using IRC +10216 as a reference assuming $T_A^* = 24$ K for IRC +10216 in CO(2–1) as determined by previous observation. The data were divided by the main beam efficiency, $\eta_{\rm MB} = 0.72$, as determined by continuum measurements of planets. Figure 2 shows a position-velocity intensity map for the data in Figure 1. Figure 3 shows an integrated intensity map for the data obtained in 1991 June.

Integration times vary from 2.6 minutes for the 12 inner positions to 5 minutes for the outer positions. Since the data were taken on different nights, there may be a relative pointing offset between individual spectra as large as 8″–10″. We checked our pointing every night by making sure that at the nuclear position, we could clearly see the sharp absorption feature at 550 km s^{-1} against the compact continuum source (Israel et al. 1990; Phillips, Sanders, & Sargent 1990), also observed in H I (van der Hulst et al. 1983) and in other molecular lines (Gardner & Whiteoak 1976; Eckart et al. 1990a; Israel et al. 1991).

3. THICKNESS OF THE GAS DISK

A first glance at the CO(2–1) spectra for the outer positions (profiles at offsets -0.90, 0.44 and 0.90, -0.44 in Fig. 1) reveals sharp edges with width less than 10 km s^{-1}. These steep edges set a limit on the velocity dispersion (effective sound speed) σ of the molecular gas clouds $\sigma < 10$ km s^{-1}. This is substantially lower than the value of ~ 60 km s^{-1} estimated by Eckart et al. (1990b) from their CO(1–0) data (see § 8 for further discussion).

Hydrostatic equilibrium of a gas disk in the equatorial plane of an axisymmetric potential to first order yields

$$\frac{h}{R} = \frac{q\sigma}{v}, \qquad (3.1)$$

where v is the velocity at radius R in the disk, h is the density

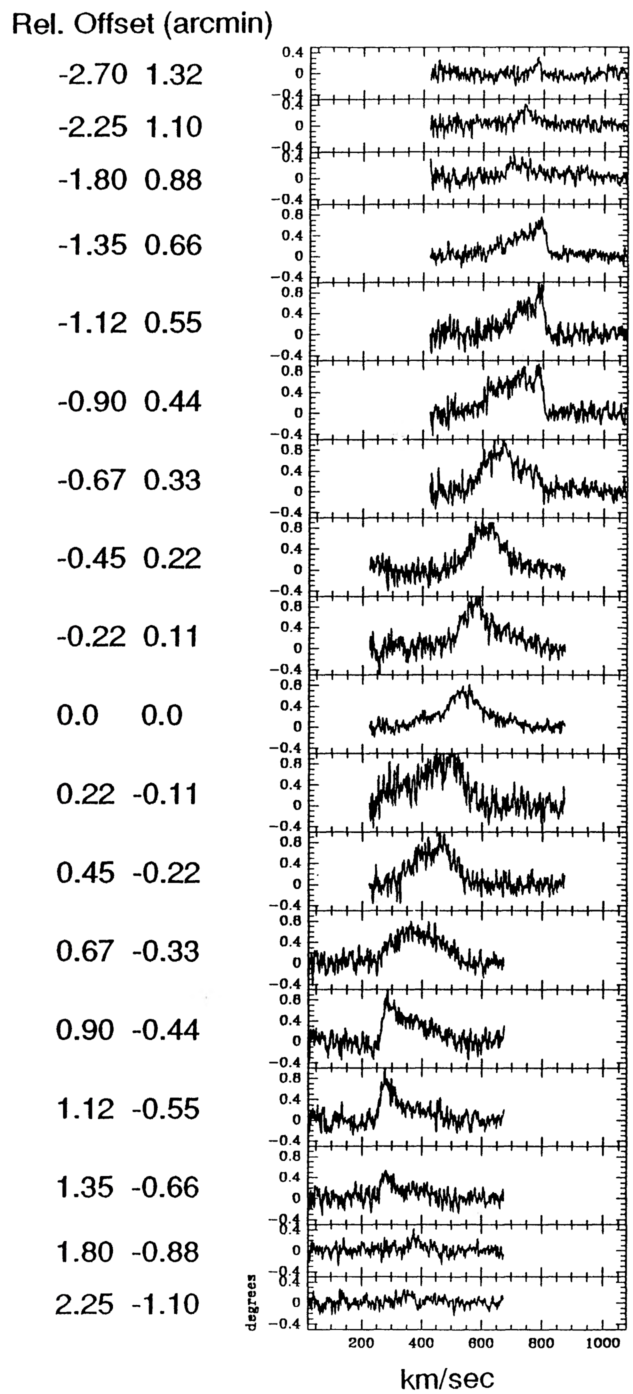

FIG. 1.—^{12}CO(2–1) spectra at PA $-63°.5$ along the dust lane of Cen A. The vertical axes give the main beam antenna temperature in K. The horizontal axis gives velocity with respect to the local standard of rest, $V_{\rm LSR}$, in km s^{-1}. Relative offsets are in arcminutes from the unresolved H I continuum source (van der Hulst, Golisch, & Haschick 1983) at R.A. = 13$^{\rm h}$22$^{\rm m}$31.65, decl. = $-42°45'32''.00$ (1950).

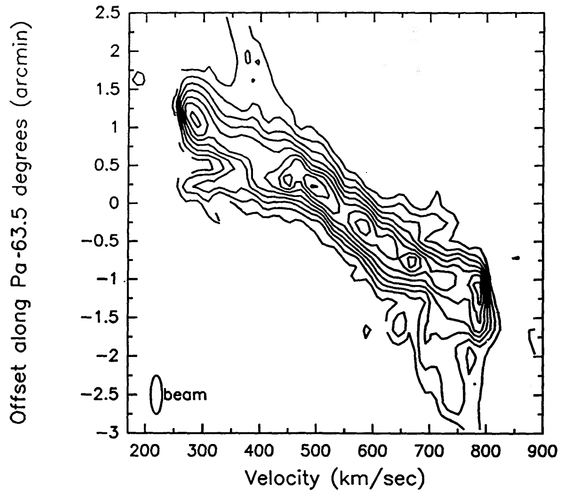

FIG. 2.—Position-velocity intensity map along the dust lane. Relative offsets are along PA −63°.5 from the nucleus of Centaurus A. Velocity resolution has been smoothed to 20 km s^{-1}. Levels begin at 0.1 K with 0.1 K intervals. The 3 σ noise temperature is approximately 0.12 K. Velocity is given with respect to the local standard of rest.

scale height of the disk, and q is the axis ratio of the potential, which, for the nearly spherical systems that we are interested in can be written approximately as a function of $R^2 + z^2/q^2$. Prolate systems have $q > 1$, while oblate systems have $q < 1$. In the central regions of Cen A where the CO is located, $q \sim 1$. Using the peaks of our outer profile shapes, for $R > 60''$ we find a minimum value for v to be 260 km s^{-1} which corresponds to a gas disk at an inclination of 90°. Using this minimum value for v, our limit $\sigma < 10$ km s^{-1} restricts the disk thickness h to less than $h/2''.5$ (35 pc) at $R > 60''$ (900 pc).[4]

Another limit on the thickness of the disk can be obtained from the observation that OB star formation is taking place in the molecular disk at the rate of $\sim 1.6\ M_\odot\ \mathrm{yr}^{-1}$ (Marston & Dickens 1988), so that the disk must be locally Jeans-unstable. This requires (e.g., Binney & Tremaine 1987, eq. [6-49])

$$\frac{\sigma\kappa}{\pi G\Sigma} < 1 , \tag{3.2}$$

where Σ is the surface density of the disk and κ is the epicyclic frequency. Assuming that the disk is on the limit of stability, and using equation (3.1), then gives

$$h \approx \frac{q\pi G\Sigma}{\Omega\kappa} , \tag{3.3}$$

[4] We use 3 Mpc for the distance to Cen A (Tonry & Schechter 1990).

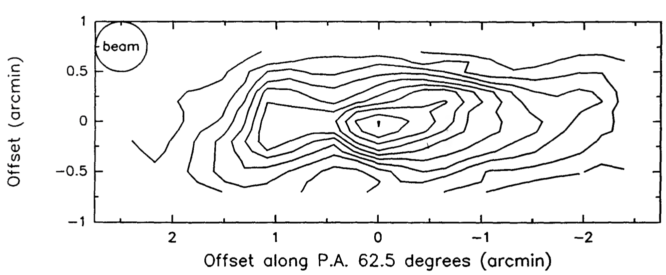

FIG. 3.—Integrated intensity CO(2–1). Contours spaced 10% apart with the lowest contour at 10% of maximum intensity. For a picture of positions observed on the sky, see Fig. 8c.

where the angular velocity $\Omega = v/R$. Since galactic disks are observed to lie within a factor of 2–3 of the stability line (Kennicutt 1989), we estimate

$$h < \frac{3q\pi G\Sigma(R = 0)}{\Omega^2(R = 90'')} , \tag{3.4}$$

over the range of our data. Whereas it is not evident that Kennicut's result for spiral disks applies to the disk of Cen A, we will show that it is consistent with the observed low velocity dispersion. Here we have used the fact that Σ is largest at $R = 0$, and that $\kappa \sim \Omega$ where the rotation curve flattens. Over the range of our data, Ω is lowest at $R = 90''$. Using $\Sigma(R = 0) = 2\text{–}3 \times 10^8\ M_\odot/[2\pi(60'')^2]$, which is a good fit to the CO(2–1) integrated intensities (Phillips et al. 1987) and $R\Omega = 260$ km s^{-1} (the asymptotic velocity which our data approaches when $R > 60''$) to obtain a lower limit for Ω at $R = 90''$, we find a limit on the thickness of the disk of $h < 25$ pc, and a limit on the velocity dispersion of the gas clouds $\sigma < 7$ km s^{-1}. These limits may be slightly low because we did not consider the fraction of the disk made up of cold (low velocity dispersion) newly formed stars (estimated from the star formation rate to be less than 10%). There should also be corrections of order unity due to the onset of two-fluid instabilities (Jog & Solomon 1984).

The small thickness of the disk that follows from the above arguments is consistent with the conclusion of BTA that the symmetry of their projected velocity field implies that they observe both sides of the disk even though the disk is highly inclined. As BTA conjectured, this is possible only if the disk is thin.

4. KINEMATIC MODELING

Previous attempts at extracting a rotation curve from the gas kinematics of Cen A include fitting the H I velocity field (van Gorkom et al. 1990), and the Hα velocity field (BTA). Van Gorkom et al. (1990) obtained a good fit to their H I data with a rotation curve that results from a model with gas on circular orbits in a spherical galaxy with a light distribution that obeys a de Vaucouleurs law. Nicholson et al. (1992) find good fits to the Hα data of BTA by using an axisymmetric model with a differentially precessing inclined circular disk. Modeling procedures such as these usually compare the data to projected model velocity fields or channel maps (e.g., Begeman 1987; Lees 1991). This is possible because of the sufficiently high spatial resolution (Hα beam $\sim 2''$) and because the data sets fully cover a large area on the sky. In regions where the rotation curve is not linear, the size of the beam also affects measurement of the rotation curve. This effect, known as "beam smearing," can significantly influence the measured shape of the rotation curve even in high-quality H I data (Begeman 1987). Because of the relatively large size of the CSO beam in the CO(2–1) line (FWHM = 30″), the mean velocity at each beam position is a weighted average over a large fraction of the disk and is not very informative. However, the full velocity profile shapes contain much information about the projected velocity field. As a result, we decided to model directly the profile shapes at each position where we took data.

Various authors have estimated the time scale for infalling gas to settle onto the simple closed orbits of a host galaxy to be about 1–3 × 10^9 yr at an effective radius (e.g., Tohline, Simonson, & Caldwell 1982; Habe & Ikeuchi 1985, 1988; Steiman-Cameron & Durisen 1988), but these values are rather uncertain (de Zeeuw 1990). We note that this time scale is approximately the same as the estimated age of the shell-like stellar features observed in the outer part of Cen A by Malin et al. (1983) and in the simulations of galaxy-galaxy collisions by Hernquist & Quinn (1988, 1989). The small velocity dispersion of the molecular gas, and the small thickness of the disk, suggest that the gas is (nearly) settled, and we therefore approximate the gas velocity field by assuming the gas occupies simple, i.e., non–self-intersecting, closed orbits in the potential of Cen A.

Our procedure consists of doing a simulated observation in which a projected model velocity field is convolved with the beam of the CSO. Around each position on the sky where we have a CO spectrum, we construct a two-dimensional grid. Simultaneously we also make an array of velocity bins. At each position on the grid the line of sight velocity is computed, and a corresponding weight is placed at that location in the velocity bin array. This weight consists of three factors:

1. A factor that depends on the distance between the point of the grid and the center of the beam. For the CSO, a Gaussian representation of the beam is accurate to the 1% level.
2. A factor that depends on the azimuthally averaged intensity of the model disk at that radius. Since the profile shapes on either side of the nucleus are quite similar (see Fig. 4*a*), nonaxisymmetric variations in intensity, such as might be caused by spiral arms, must not be large enough to significantly affect the observed profile shapes. This may be because of the high inclination of the gas disk and the large beam size.
3. A factor which is necessary only for gas either on noncircular orbits or in a warped disk. For gas on closed noncircular orbits (§ 6), this third factor is a surface density correction resulting from the continuity equation and the variation of the gas velocity along the orbit, while for gas in a warped disk (§ 7), this factor depends on the inclination of the gas disk with respect to the line of sight at the point under consideration.

The resulting velocity array is a model profile shape that incorporates the finite size of the CSO beam and can be compared directly to the observations. Since a specific line-of-sight velocity is computed at each position on the grid, not a spread of velocities, we have assumed that the gas disk is infinitely thin and has no velocity dispersion. The limits on the dispersion set in § 3 imply that this should be a very good approximation. The width of the modeled profile shapes results from the finite size of the beam, not the velocity dispersion of the gas clouds.

We discovered that a least mean squared (χ^2) fitting routine is not particularly useful for fitting models to our data. The large number of data points and the numerical nature of the convolution make it time consuming to use a fitting routine which must try out many different models before converging. Although a first glance it seemed that the parameter space was large, we discovered that the fitting is mostly sensitive to two or three parameters, with some of the others heavily constrained by these, and the remaining ones having little influence on the fits. As a result, we manually explored parameter space. Instead of listing formal errors on the derived parameters, we list ranges in which we have found adequate fits to the data. Since our data consist of 57 one-dimensional velocity profile functions, i.e., many hundreds of independent numbers, fitting models requiring 6 to 10 parameters is not unreasonable. Quality of fit was judged both by χ^2 and by consistency with other observations of Cen A such as the position angle of the optical isophotes of the underlying galaxy.

5. CIRCULAR ORBITS IN A PLANE

We start with the simplest models for the CO gas kinematics and assume the gas is on circular orbits in a plane.

5.1. *Rotation Curves*

We examine two families of models with simple rotation curves. The first set has a rotation curve given by

$$v_c(R) = \frac{AR}{(R^2 + c^2)^{1/2}}, \qquad (5.1)$$

where A and c are parameters. This rotation curve corresponds to Binney's (1981) logarithmic potential with finite core radius c, and we therefore refer to models of this kind as Binney models. The rotation curve rises linearly in the homogeneous core ($R \ll c$), and asymptotically approaches the value A at large radii, so that the models have infinite total mass. This does not affect our fits because the CO emission is confined to the rising part of the rotation curve. We note that an asymptotically flat rotation curve is not inconsistent with the H I data at larger radii (van Gorkom et al. 1990).

To verify that our conclusions are not unique to models with a finite core radius, we also consider the rotation curve of Hernquist's (1990) spherical model which is a good approximation to a de Vaucouleurs galaxy. In this case the associated density profile diverges as $1/r$ in the center, where r is the spherical radius. The rotation curve is given by

$$v_c(R) = \frac{\sqrt{GMR}}{R + r_0}, \qquad (5.2)$$

where G is the gravitational constant, M is the total mass, and r_0 is the scale length of the model. The half-light radius r_e is equal to $1.8153 r_0$. We have replaced r by the cylindrical radius R to indicate that we are interested only in the rotation curve in the equatorial plane ($z = 0$) and do not require that the potential of Cen A is in fact spherical. The rotation curve rises very steeply in the central region ($R \ll r_0$), reaches a maximum at $R = r_0$, and decreases as $1/R^{1/2}$ at large radii.

Figure 4 shows profile shapes, projected velocity field, projected intensity contours, and projected orbits for the Binney model. Though we investigated both models and will discuss both, the profile shapes for the two models are not significantly different, and we include only a figure for the Binney model. The models are normalized such that the peaks of the outer profiles match the peaks of the data; this means adjusting A for the Binney models and M for the Hernquist models. For the Binney models the core radius c was varied also for finding the best fit. For the Hernquist models we could have varied r_0, but we decided to fix it by the observed value of 305″ for the half-light radius of Cen A (Dufour et al. 1979). The intensity of the CO(2–1) disk as a function of radius R in the disk was assumed to be a Gaussian, $\exp(-R^2/2\sigma_s^2)$ with $\sigma_s = 65''$ which is consistent with the observed radial distribution of CO(2–1) (Phillips et al. 1987). V_{sys} was also adjusted. Finally, both the inclination of the disk, ϑ, and the position angle χ of the projected short axis to the gas disk were varied for best fit.

We obtained $V_{sys} = 540 \pm 5$ km s^{-1} with respect to the local standard of rest[5] (532 ± 5 km s^{-1} heliocentric) for both models. The inclination $\vartheta = 80° \pm 3°$, and the position angle of

[5] Velocities in this paper are taken to be $(\Delta\nu/\nu_0)c$, where c is the velocity of light, ν_0 is the rest frequency, and $\Delta\nu$ is the frequency shift of the line observed. The difference between our velocity and the optical convention $(\Delta\lambda/\lambda_0)c$ at Cen A is approximately 1 km s^{-1}.

FIG. 4*a*

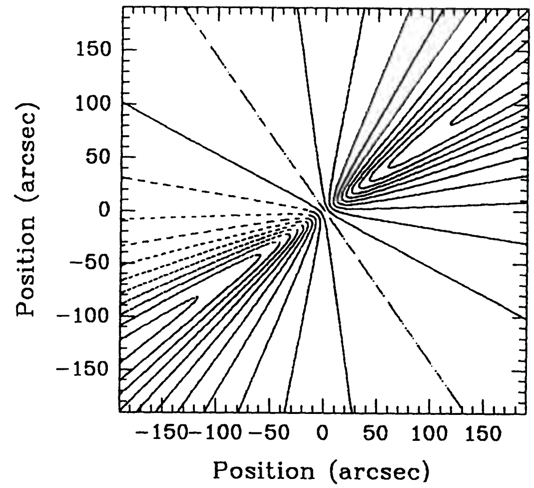

FIG. 4*b*

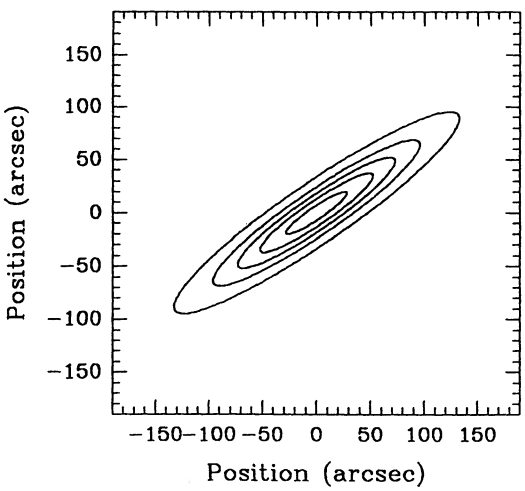

FIG. 4*c*

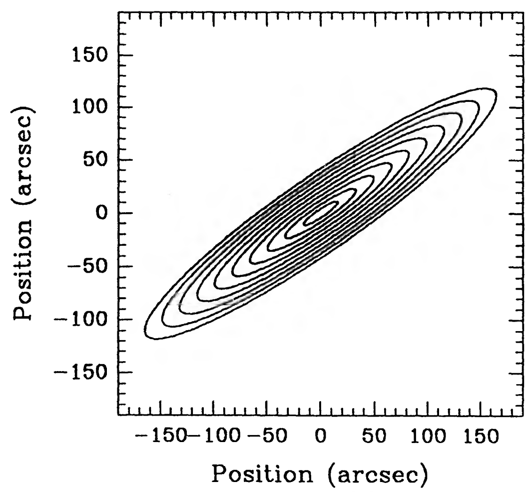

FIG. 4*d*

FIG. 4.—(*a*) Best-fit model with circular orbits and a Binney rotation curve. Solid lines are the data; dotted lines are the model. Each profile displayed is located at a different position on the sky with the central profile at the nucleus. The spacing is 30″ along PA −63°.5 which is the horizontal direction in the figure and is 15″ along PA 26°.5 which is the vertical direction in the figure. See Fig. 8*c* for a picture of the beam positions on the sky. The vertical axes give the main beam antenna temperature in K and range from −0.1 to 1.0 K. The horizontal axes give velocity with respect to the local standard of rest, V_{LSR}, and range from 170 to 900 km s^{-1}. See text and Table 1 for parameters of the model. (*b*) Projected velocity field, Contours are 25 km s^{-1} apart. The dot-dash contour is at the systemic velocity V_{sys}. The dotted contours are at velocities less than V_{sys}, and the solid ones indicate velocities larger than V_{sys}. (*c*) Intensity contours. Levels are 20% apart and range from 20% to 100% of maximum intensity. (*d*) Projected orbits. Contours are 20″ apart and are the radius on the gas plane as seen on the sky. The vertical direction is north.

the short axis of the disk $\chi = 35° \pm 5°$ are constrained tightly. There are no significant differences between the best fits of the two different models. This is not surprising because our spatial resolution is poor; the large beam effectively averages over the range where the two velocity curves are different so that the resulting model profiles differ little.

The parameters of the best-fitting Binney model (Fig. 4) are $A = 290 \pm 20$ km s^{-1} and $c = 40'' \pm 15''$. This corresponds to a mass of $1.1 \times 10^{11}\ M_\odot$ inside 4.5 kpc ($1.2r_e$). The best-fitting Hernquist model has total mass $M = 2.8 \times 10^{11}\ M_\odot$. For the assumed value of r_0, this gives $1.3 \times 10^{11}\ M_\odot$ inside $1.2r_e$. These masses agree with that derived by van Gorkom et al. (1990) by fitting a velocity curve appropriate for a de Vaucouleurs law to the H I data. We find as they do, that the rotation curve in this region is consistent with a roughly constant mass-to-light ratio which is approximately 3 in solar units. Since our CO(2–1) measurements do not extend beyond 1.5 kpc, the above result merely confirms that the CO velocities are consistent with the H I velocities measured at larger radii, a result which is evident on comparing the position-velocity diagrams for both species directly.

5.2. *Temperature and Filling Factor*

Our value for the inclination of the disk allows us to estimate T_n, the temperature that would be observed if a plane of gas that is at uniform velocity with respect to the observer and is of the same temperature and filling factor as the disk were observed face-on.

$$T_n = f_a T_c = \frac{\cos \vartheta}{A(v)} T(v) , \tag{5.3}$$

where $T(v)$ is the antenna temperature observed at velocity v, $A(v)$ is the fractional area of the beam covered by gas emitting at this velocity, T_c is the average temperature of the clouds from which the disk is formed, and f_a is the effective area filling factor of these clouds. We have $f_a = f_v h/r_c$, where f_v is the volume filling factor of the gas clouds, r_c is the radius of the typical cloud and h is the thickness of the disk. Using equation (5.3) we estimate $f_a T_c \approx 1.2$ K for the central position observed and $f_a T_c \approx 0.3$ K for the position observed at $r = 60''$. Assuming $T_c \approx 10$ K (Eckart et al. 1990b), the area filling factor f_a then ranges from 0.03 to 0.12, with slightly lower filling factors for $r > 60''$. For a thin disk, f_a is roughly the same order as f_v, so that these values are consistent with the hypothesis that the molecular material of Cen A is clumpy and has filling factor and average cloud temperature similar to the molecular material of our Galaxy. Such a low filling factor implies that it is possible to see through the disk, even at inclinations larger than 80°. This is consistent with the hypothesis of BTA that the Hα disk is optically thin.

5.3. *Defects of Circular Orbit Models*

It is clear from the fit shown in Figure 4 that our method of modeling the profile shapes is a promising one. The overall profile shapes can be reproduced reasonably well by convolving a projected model velocity field with the CSO beam. The widths of the profile shapes can be reproduced with only a small cloud velocity dispersion. However, there are a number of discrepancies in detail. We discuss them in turn.

Inspection of Figure 4 reveals that positions 30″ to the east and west of the nucleus have mean velocities further from the systemic velocity than observed, although the Binney model fits slightly better than the Hernquist model at these positions. This is due in part to the fact that c was treated as a free parameter for the Binney model, whereas we fixed r_0 for the Hernquist model. Thus, the Binney model has an extra degree of freedom to match the radius at which the velocity curve rounds off. Possibly, the rotation curves that we have chosen are too steep in the central region and do not round off sharply enough. However, significantly changing the shape of the rotation curve would not be consistent with the observation that the radial intensity in the infrared (K) of the central region follows a de Vaucouleurs law to within 1″–2″ of the nucleus (Giles 1986; Frogel, Quillen, & Graham 1992).

The velocity centroids of positions to the north and south of the nucleus are reproduced incorrectly by the circular models. As is clear from the projected velocity field in Figure 4*b*, the models have mirror symmetry with respect to two axes. The zero velocity curve, i.e., the contour at the systemic velocity, is a straight line. The maximum velocity curve is also a straight line, which is perpendicular to the zero velocity line. This is true for any flat circular disk, so changing the rotation curve will not improve the fit at these positions.

The intensities of positions to the north and south of the nucleus are higher than those produced by the models. This could be because we have overestimated the FWHM of the intensity as a function of radius on the disk, or because the inclination of the models is too high. It is impossible to correct for these effects with the circular models since lowering the inclination makes the profile shapes at positions in the inner part of the disk too thin, and increasing the FWHM of the intensity curve makes the profile shapes at positions to the east and west of the nucleus too large.

The position angle χ of the short axis of the gas disk is 35° for the best circular fits. This coincides with the position angle ϑ_s of the photometric major axis of Cen A, which is measured in the optical by fitting ellipses to the isophotes for $70'' < R < 255''$ to be at $\vartheta_s = 35 \pm 3°$ (Dufour et al. 1979). Although our kinematic fit is consistent with placing the disk perpendicular to this axis, neither the dust lane nor the major axis of the CO isophotes are observed to be perpendicular to the photometric major axis. Optically the dust lane is measured to be at roughly PA 116°, whereas the position angle ϑ_d of the major axis of the CO intensity contours varies from $\sim 116°$ in the inner region to $\sim 125°$ beyond 70″ (see Fig. 3). Our best-fitting circular models have $\vartheta_d = 125°$. Either the gas is not in a principal plane of the galaxy, in which case it would be warped due to differential precession, or it is in a principal plane and our observation of a misaligned gas disk is a projection effect due to the triaxial nature of the galaxy (e.g., Stark 1977). In the latter case, we would expect noncircular motions.

We show in the following sections that models with a warped geometry of the disk or with noncircular motions have projected velocity fields that are twisted, similar to what is observed in Hα (BTA). This results in wider profile shapes, systematic shifts in the velocity centroids and gas intensity contours that are not aligned with the projected principal axes of the galaxy. Nevertheless, we find that planar models even with noncircular motions cannot fit the observed CO line profiles while simultaneously explaining the observed orientation of the starlight and gas isophotes. With a warped model, by contrast, we obtain an excellent and predictive fit.

6. NONCIRCULAR ORBITS IN A PLANE

In this section we investigate the possibility that the gas is in a principal plane, and that the misalignment discussed in the previous paragraph is the result of projection of a triaxial stellar density profile. The simple closed orbits for the cold gas are then no longer circular, but are roughly elliptic. If the figure of the galaxy does not tumble, the orbits can lie either in the plane perpendicular to the short axis or in the plane perpendicular to the long axis of the galaxy.

6.1. *Mass Models and Viewing Angles*

We have used two different kinds of triaxial models. The first are separable (Stäckel) models, which are typical of models with homogeneous cores. The simple closed orbits are exact confocal ellipses, and the velocity field can be given by simple analytic expressions (ZF). In the core, the confocal ellipses become highly elongated, and the closed orbit approximation for the gas kinematics becomes unphysical. The specific mass models we have used are the $p = 1$ members of the family described in Appendix B of ZF. In the axisymmetric limit, their rotation curve reduces to that of the Binney model, given in equation (5.1).

The second set of models is defined by taking the potential of the spherical Hernquist model and adding two spherical harmonic terms with a radial fall-off such that the associated density becomes triaxial with roughly elliptic isophotes (see Appendix). The detailed properties of the models are given in Lees & de Zeeuw (1991, hereafter LZ). These models again have a central cusp, and the axis ratios in the center and at large radii can be chosen freely. The closed orbits can be calculated with first-order epicyclic theory (e.g., Gerhard & Vietri 1986) and reach a finite elongation in the center. This approximate description is sufficiently accurate for moderately flattened mass models (LZ), specifically those with axis ratio less than 0.5 on the plane in which the gas is located.

Three viewing angles are needed to specify the orientation of a triaxial galaxy. We choose Cartesian coordinates (x, y, z) along the three principal axes of the system, and we assume the gas is in the (x, y)-plane. Following the convention of ZF (see their Fig. 2), we take ϑ and φ as the usual spherical polar angles of the line of sight, so that as in § 5, ϑ is the inclination of the gas plane, i.e., the angle between the line of sight and the z-axis. For $\vartheta = 0°$ the disk is face-on, and for $\vartheta = 90°$ the disk is edge-on. The angle χ is again the position angle on the sky of the projected z-axis, measured from the north.

We remark that ZF defined the long axis of the galaxy to be always in the x-direction and the short axis to be in the z-direction, and then discussed models with gas in the (x, y)-plane and models with gas in the (y, z)-plane separately. By contrast, we assume the gas is always in the (x, y)-plane and vary the axis ratios of the galaxy (see also Bertola et al. 1991). If a, b, and c denote the semi-axes along the x, y, and z directions, respectively, then ZF have $a > b > c$ always, but we consider both $a > b > c$ and $c > a > b$.

For a triaxial system with ellipsoidal surfaces of constant density, the apparent axis ratio b'/a' of the projected surface density, and the value of Θ^*, the position angle difference between the apparent major axis and the direction of the zero velocity curve at large projected radii, are both functions of the intrinsic axis ratios b/a and c/a and the viewing angles ϑ and φ. ZF (Appendix A) have shown that for given viewing angles ϑ and φ, the observed values of Θ^* and b'/a' may be used to calculate explicitly the corresponding axis ratios b/a and c/a. Once these are known, the gas velocities can be calculated. Thus, in order to fit the velocity fields, we vary the same parameters as for the circular models: A and c for the separable models, and M for the modified Hernquist models. Measurement of Θ^* is difficult from the Hα velocity field, because the zero velocity line is noisy, and because the zero velocity line may not converge asymptotically to a straight line over the scale of this map, though we estimate $\Theta^* = -5° \pm 20°$. As a result Θ^* was among the parameters varied. Also varied were the angles ϑ and χ, and the axis ratio of the potential on the (x, y) (gas) plane. The observed value for b'/a' then fixed the other axis ratio and φ. In addition, for both types of models, the systemic velocity V_{sys} is varied.

6.2. *Triaxial Models with Constant Ellipticity*

Although the optical isophotes of the inner part of Cen A are observed to be round (Dufour et al. 1979), the near-infrared K isophotes have axis ratios of $b'/a' = 0.8$ to within 70″ of the center. Van den Bergh (1976) has suggested that star formation in the disk is responsible for the rounding of the optical isophotes. We first set $b'/a' = 0.8$ and postpone a discussion of models with changing ellipticity to § 6.3.

Gas clouds on closed noncircular orbits are not uniformly distributed around each orbit, because the equation of continuity $\nabla \cdot \Sigma_g \boldsymbol{v} = 0$, where Σ_g is the surface density of the gas, and $\boldsymbol{v}$ is the velocity vector, requires the surface density to vary. We assume that the intensity is proportional to Σ (nonoverlying clouds) and compute the azimuthal variation of Σ_g from the equation of continuity (see ZF, eq. [2.12]). Σ is assumed to decline as a Gaussian function of the semimajor axis of the orbits (see § 5.1), with dispersion $\sigma_s = 60''$.

Figure 5 displays our best-fit Stäckel model, which has $A = 300 \pm 10$ km s^{-1} and $c = 40'' \pm 15''$, and axis ratios a:b:c = 1:2:2.6, so that the model is prolate/triaxial. The best-fitting viewing angles are $\chi = 37° \pm 5°$, $\vartheta = 80° \pm 3°$, $\varphi = 20° \pm 8°$. Furthermore, $V_{sys} = 538 \pm 5$ km s^{-1} with respect to the local standard of rest ($V_{sys} = 541 \pm 5$ km s^{-1} heliocentric). The peculiar intensity contours in the center of the model (Fig. 5c) are caused by the unphysical nature of the closed orbit approximation in the center (ZF). Since this effect is averaged over the center beam and affects only the center data position, it does not significantly influence our profile shapes or fits, and we ignore it. Figure 6 is our best-fit modified Hernquist model. Only the projected velocity contours and intensity contours are shown since the modeled profile shapes are very similar to those of the Stäckel model. The angular parameters are identical to the parameters for the separable model. The total mass within 4.5 kpc for these models is roughly the same as that of the circular models discussed in § 5.

When gas is on noncircular orbits, there is a component of the velocity in the direction toward the center of the galaxy. When the line-of-sight velocity is compared with that of a circular orbit, this component has the effect of increasing the line-of-sight velocity on two quarters of the orbit and decreasing it on the others. The angle φ determines which part of the orbit has increased line-of-sight velocity. The models with low φ, in which the orbits are seen roughly broadside-on, produce the best fits because the ellipticity of the orbits reduces the velocities at positions to the east and west of the nucleus. Compared with the circular orbit models of § 5, the noncircular model improves the fit at these positions. However, the fit at positions to the northwest and southeast of the nucleus is not improved. Although these models provide no better global fits than the circular model, they are more consistent with other observations of Cen A which are discussed in the following paragraphs.

For our best fits the position angle of the isophote major axis $\vartheta_s = 32°$ is consistent with that observed, $\vartheta_s = 35° \pm 3°$ (Dufour et al. 1979). This implies that the potential axes are at the same orientation in the inner region of the galaxy where there is CO emission as they are in the outer region where the starlight isophote axes can be measured. This is consistent with the fact that no isophote twist has been observed in Cen A.

The position angle ϑ_d of the major axis of the gas isophotes (Figs. 5c and 6b) of the model is $\sim 125°$ for $R > 60''$, as in the circular models, but in addition ϑ_d twists to a lower position angle in the central regions ($R < 60''$) as observed (see Fig. 3). However, in the central regions, ϑ_d is observed to be 116°, whereas the model has $\vartheta_d \sim 121°$. Although the noncircular orbit model matches the observations in the outer part as well as the circular orbit models do, and qualitatively matches the observations in that ϑ_d becomes lower in the central regions, it does not agree completely with the observations. This could be because we have used too simple a model for the intensity as a function of radius (a molecular ring would also change the observed angle of disk isophotes in the center).

There are a few qualitative features of interest in these noncircular models. The zero-velocity line (the systemic velocity contour on the projected velocity contour plots) in these models is curved and not aligned with the position angle of the axis perpendicular to the gas plane on the sky (see Figs. 5b and 6a), whereas for the circular models, the zero-velocity line is straight and aligned with the projected short axis of the disk. The maximum velocity curve for the noncircular models is not perpendicular to the zero velocity curve. Since the velocity field does not have mirror symmetry, there is a higher density of

FIG. 5a

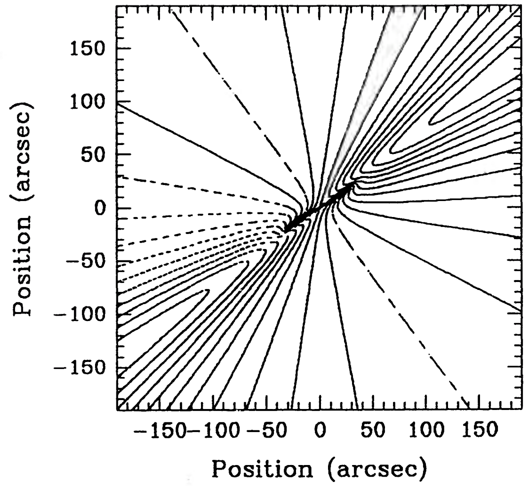

FIG. 5b

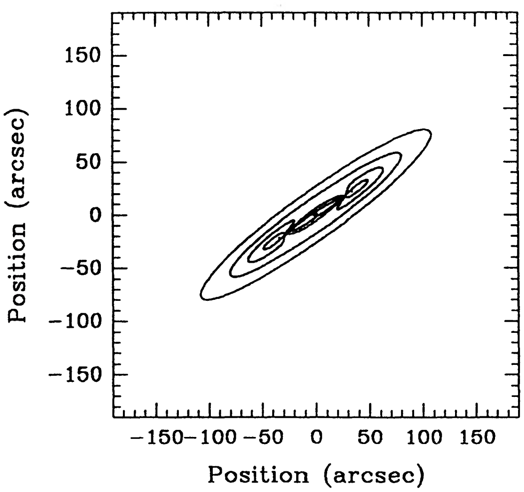

FIG. 5c

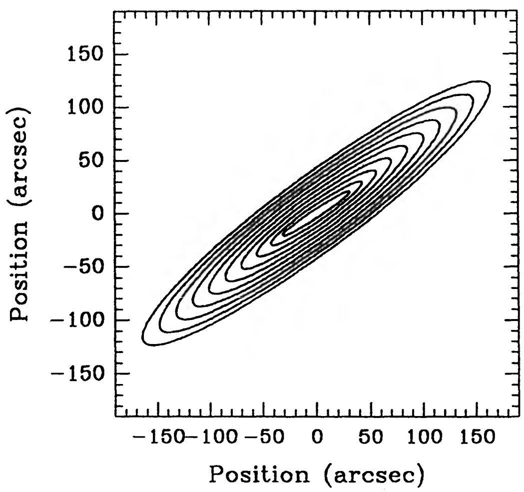

FIG. 5d

FIG. 5.—Best-fit triaxial Stäckel model. (*a*) Profiles. (*b*) Projected model velocity field. (*c*) Model intensity contours. (*d*) Projected closed orbits for the gas. See Fig. 4 legend, Table 1, and text for further details.

contours per unit area of the velocity field. Because of this, each beam sees a larger velocity range, and the profile shapes are slightly wider. Unfortunately, most of the effects of noncircular motion are masked in Cen A by the high inclination of this particular system. This is because most of the twisting of the velocity field contours is concentrated in a small area on the sky, so that the effects of the noncircular motion are averaged away by the finite resolution of observation. Large deviations from circular motion would be more apparent in a system with a less inclined gas disk.

6.3. *Triaxial Models with Changing Ellipticity*

Changing the axis ratios of the triaxial model as a function of radius such that the isophotes become flatter with increasing radius makes the closed orbits for the gas more circular in the center and less circular in the outer regions of the gas disk. The resulting maximum velocity line will curve out further away from the minor axis of the galaxy in the outer region. We therefore investigate the possibility that a model with changing ellipticity could account for the curved maximum velocity line observed in Hα (BTA) and to see if our profile shapes can be better fit with such a model.

We use the modified Hernquist models so that the effects of the changing ellipticity in the central region are not obscured by the unphysical nature of the Binney models in this region. We set Θ^* to be constant, so that the isophotes do not twist, and vary the observed b'/a' as a function of radius. We find that the maximum velocity line for these models does indeed twist. A slightly twisted maximum velocity curve could be modeled by a triaxial model with changing axis ratios, though a severely twisted one cannot be modeled this way. Thus these models are qualitatively right, but none of them have a twist in the maximum velocity line as large as that observed in the Hα data. No model was found that fits our data better than the modified Hernquist models of § 6.2. The higher the inclination of the system, the less freedom there is to model twists in the velocity contour map as a triaxial system with gas on noncircular orbits (assuming that the axis ratios of the triaxial system are all greater than 0.3). This is because at high inclination, the twisting of the velocity field is concentrated in a much smaller area on the sky.

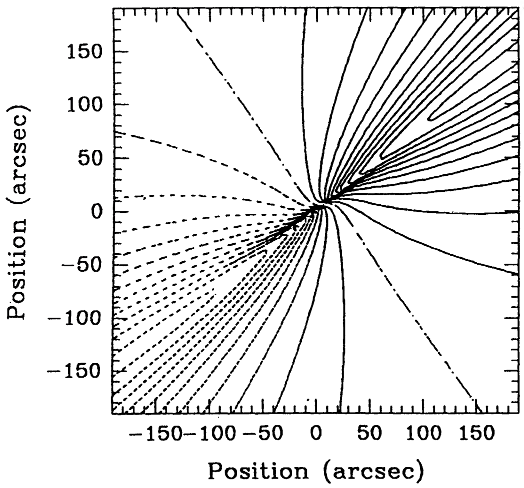

FIG. 6*a*

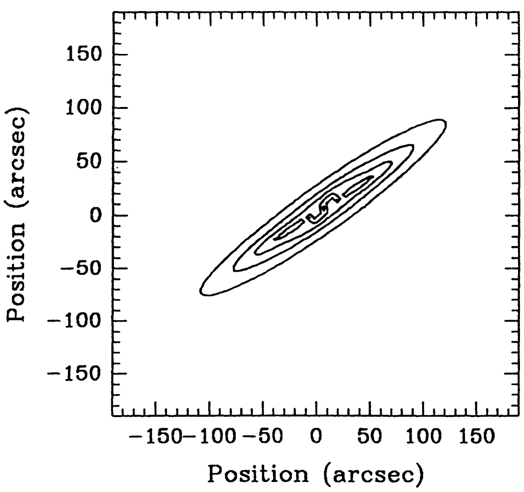

FIG. 6*b*

FIG. 6.—Best-fit modified Hernquist model. (*a*) Projected model velocity field. (*b*) Model intensity contours.

7. WARPED DISKS

In this section we return to axisymmetric models, but relax the constraint that the gas lie in the equatorial plane, and consider warped configurations.

7.1. *Tilted Rings*

For gas close to the equatorial plane in a moderately flattened axisymmetric potential, we can think of a warp as a set of smoothly connected inclined rings, where each ring is centered on the nucleus of the galaxy with radius r the distance from the nucleus (e.g., Sparke 1986). We describe the geometry and orientation of the warp with four angles, two of which are a function of r. We again use the angles χ and ϑ to describe the orientation of the axisymmetric potential. We denote by z' the rotational axis of symmetry of the ring at radius r, and let ω be the angle between the z- and the z'-axis. We define α to be the angle in the equatorial plane of the projection of z' onto this plane minus the angle of the projection of the line of sight (see Fig. 7). A disk which was once in a single plane inclined with respect to the principal plane of the potential will at a later time have undergone differential precession. If there has not been settling onto the principal plane of the potential, then at this later time ω will be constant and α will vary as a function of r.

Previous work on fitting a collection of tilted rings to kinematic data involved simultaneously fitting continuous curves for the inclination and the precession angle as a function of r (e.g., Begeman 1987; Staveley-Smith et al. 1990). We attempted instead to find a set of simple curves for $\alpha(r)$ and $\omega(r)$ so that we can fit our data with a few parameters instead of fitting $\alpha(r)$ and $\omega(r)$ as continuous curves. Our first experiment was to see if we could fit our observations with a disk of constant inclination (ω constant) that is warped as a result of differential precession. This simple model is identical to the one used by Tubbs (1980) to model the morphology of the optical dustlane. In an axisymmetric potential of ellipticity $\epsilon_p = 1 - 1/q$, where q is the axis ratio of the potential as defined in § 3, the precession rate $d\alpha/dt$ is approximately

$$\frac{d\alpha}{dt} \sim \frac{\epsilon_p v}{r} . \tag{7.1}$$

The precession is prograde for a prolate potential ($q > 1$) and is retrograde for an oblate potential ($q < 1$). Assuming that the disk is initially in a plane at constant inclination [$\omega(r)$ constant], and that there is minimal settling onto the principal plane, minimal inflow, and ϵ_p is constant as a function of time, after a time Δt

$$\alpha(r) = \epsilon_p \Omega\, \Delta t + \alpha_0 . \tag{7.2}$$

If this model is to apply, the direction of the warp on the Hα projected velocity field (see BTA, Fig. 5 and Plate 2) implies that $d\alpha/dr < 0$. This assumes that the axis of symmetry of the potential (z-axis) is pointing toward us, where the direction of the z-axis is determined by ensuring that the rotation of the disk when projected on to the equatorial plane is counterclockwise. This implies that for Ω roughly constant and with the z-axis pointing toward us, either the galaxy in the central region is oblate ($\epsilon_p < 0$), or the galaxy is prolate and ϵ_p is decreasing as r increases so that $d\epsilon_p \Omega/dr < 0$ over the range of the Hα data. We consider two types of models: oblate models

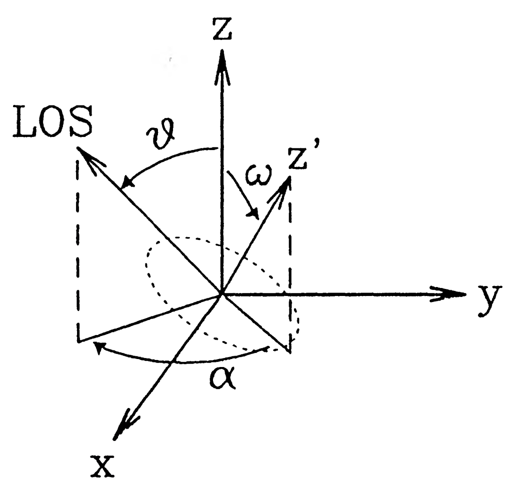

FIG. 7.—Definition of angles used in the warped disk models. The x, y, and z axes principal axes of the potential. The z' axis is the axis of symmetry of the ring represented by the dotted ellipse. LOS is the line of sight. See text for further details.

with constant ϵ_p and prolate models with $\epsilon_p = \epsilon_\infty[1 - \exp(-r^3/\sigma_e^3)]$, where σ_e is a parameter that we can roughly estimate from the infrared (K) isophote axis ratios, $40'' < \sigma_e < 80''$ (Frogel et al. 1992). We used a cubic exponential because we did not obtain good fits to our data with smoother, less steep functions.

7.2. *Projected Velocity Field*

Changing coordinates from the coordinate system of the gas disk to sky coordinates consists of doing four rotations, one for each of the angles χ, ϑ, $\alpha(r)$, and $\omega(r)$. This angle $i(r)$ between the axis of rotation z' for a disk of radius r and the line of sight is given by

$$\cos i = \cos \vartheta \cos \omega - \cos \alpha \sin \vartheta \sin \omega , \qquad (7.3)$$

where $\cos i$ is the component of the z'-axis in the direction of the line of sight. Note that $i(r)$ is not the inclination of the surface. The projection of the z'-axis on the sky is at position angle $\beta(r)$ given by

$$\sin (\beta - \chi) = \frac{\sin \alpha \sin \omega}{\sin i} . \qquad (7.4)$$

The zero-velocity line of the projected velocity field is the set of points $[r \sin i(r), \beta(r)]$, where $r \sin i(r)$ is the distance on the projected velocity field from the point to the nucleus and $\beta(r)$ can be read off as the position angle of the vector from the nucleus to the zero-velocity point on the sky. The maximum velocity line on the projected velocity field is the set of points $[r, \beta(r) + (\pi/2)]$. Information about the inclination of z' as a function of r can be found by matching points on the maximum velocity line and the zero-velocity line that are perpendicular to each other on the projected velocity field. Specifically, if $D(r)$ is the distance to points on the zero-velocity curve that are perpendicular to points on the maximum velocity curve that are r away from the nucleus, then $D(r)/r = \sin i(r)$. If the disk is folded with respect to the line of sight (see below), accurately measuring $D(r)$ may be difficult since the zero velocity line may loop; in other words, it is possible that $dD(r)/dr < 0$. It may also be difficult to locate accurately the maximum velocity line since it too may be obscured by the folding of the disk and the finite resolution of the observed projected velocity field. We note that these equations will not be accurate for gas on noncircular orbits.

For a potential with nonzero inclination ($\vartheta \neq 0$) and a gas disk with $\omega(r) \neq 0$ and varying $\alpha(r)$, generally the line of sight intersects the disk more than once. If the gas is clumpy with a low filling factor, we will see through the gas disk to other parts of the disk. In fact, splitting of the Hα line (emission from different places of the disk at one position on the sky) has been observed in the Hα spectra of Cen A (BTA). In order to generate profile shapes, it is therefore necessary to convolve the beam of the CSO with each fold of the disk separately, since clouds on different folds contribute independently to the profiles. As described in § 4, the algorithm for convolving the beam with the projected velocity field involves assigning the projected velocity field at each point on the sky a weight consisting of three factors. The first two factors are identical to those used in § 4. The third factor is necessary for a disk with changing inclination, and equals the Jacobian $J = \partial(x, y)_{\rm disk}/\partial(x, y)_{\rm sky}$, where $(x, y)_{\rm disk}$ is a local Cartesian coordinate system on the disk and $(x, y)_{\rm sky}$ is a Cartesian coordinate system on the sky. A point at which the line of sight is tangent to the surface of the disk has $1/J = 0$. A locus of such points will form a boundary, where on one side of the boundary the line of sight will intersect the disk two more times than on the other side of the boundary. Since J diverges at these points, it is necessary to use a cutoff $J \leq J_{\max}$, where $J_{\max}$ is the maximum intensity that a disk can have at the points where it folds.

We observed that models with $J_{\max} > 20$ produced spikes in the profiles that were not observed in our data set. These spikes resulted from the large intensities from the points at which the disk folded over as seen from the line of sight. This maximum allowable value for $J_{\max}$ allows us to put limits on the thickness of the disk or on the filling factor of the disk, depending upon whether the folds are optically thick (meaning that it is not possible to see through them) or optically thin. At a fold of curvature r, the line of sight intersects the disk with length approximately $(rh)^{1/2}$. The disk will be observed to be optically thick when the intersection of the line of sight with the disk is approximately of length h/f_a, where f_a is the effective area filling factor of the gas clouds of the disk, and h is the thickness of the disk. By comparing these two lengths we see that

$$f_a^2 < h/r , \qquad (7.5)$$

if the disk is to be optically thin at the folds. Using our previous estimates for h and f_a discussed in §§ 3 and 5.2, $0.03 < f_a < 0.12$, we find that the disk is optically thin at the folds. However since these estimates are not very accurate, it is possible that the folds are optically thick, though since f_a is low, it is likely that the disk is optically thin everywhere else. Therefore, we discuss both cases.

For optically thin folds $J_{\max} \approx (r/h)^{1/2}$. Our limit $J_{\max} < 20$ implies that $r/h < 400$ which gives us a lower limit for h, the thickness of the disk, and σ, the velocity dispersion of the gas clouds making up the disk, $h > r/400$ or $\sigma > v/400$ for r where there are folds at positions where we took data. Our limit of $J_{\max} = 20$ is equivalent to antenna temperatures of ≈ 23 K. Since the maximum temperature at these points cannot be greater than the expected temperature of the clouds themselves which we estimated to be ≈ 10 K (§ 5.2), we adopt the limit $J_{\max} = 10$ for our modeling.

For optically thick folds $J_{\max} \approx 1/f_a$. Our limit of $J_{\max} < 20$ implies that $f_a > 1/20$. Since we find that $f_a \approx 0.1$ over the region where the disk is observed to fold for our models (see Figs. 8 and 9), we can set $J_{\max} = 10$ once again. In this way our modeling is independent of whether the disk is optically thin or thick at the folds.

We remark that in both the optically thick and optically thin case, using a cutoff for the intensity $J_{\max}$ is an approximation. However, the fraction by which the intensity is overestimated is small and the area on the sky where this occurs is small compared to our beam size, so that the modeled profile shapes should not be much affected by this approximation. Obscuration of one part of the disk by another will cause an asymmetry in the projected velocity field: in other words the symmetry $r \to -r$, $v \to -v$ will be broken. Since the Hα projected velocity field is highly symmetrical, this effect cannot be large, consistent with the low covering factor and high clumpiness we derive. For more detailed models, it will be necessary to take into account obscuration of one part of the disk by other parts of the disk.

7.3. *Oblate and Prolate Models*

Using equations (7.3) and (7.4), rough constraints and starting points for fitting the CO profiles can be found from the Hα

projected velocity field. At the radius r_z where the maximum velocity line crosses the line on the sky perpendicular to χ, $\alpha(r_z)$ is either 0 or 180° and

$$\vartheta + \omega(r_z) \cos \alpha(r_z) = i(r_z) . \tag{7.6}$$

At the radius r_m where angle between the maximum velocity line and χ is smallest, $\alpha(r_m) = \pm 90°$, and

$$\vartheta = i(r_m) \quad \text{and} \quad \beta(r_m) = \omega(r_m) . \tag{7.7}$$

Applying these constraints to the Hα velocity field, we find that $r_z \sim 100''$, $r_m \sim 60''$, and for $\omega(r)$ constant we find that $\omega = \beta(r_m) = \vartheta - i(r_z) \sim 25°$ and $\vartheta = i(r_m) \sim 60°$. We used these values as starting points for fitting and to solve for $\epsilon_p \Delta t$, and α_0 for our models.

For our tilted ring models, we used the Binney velocity curve (eq. [5.1]) with $c = 40''$ and we took χ to be $35° \pm 5°$. The parameters in common with the circular models of § 5 were chosen to be roughly the same values as those for the best-fit circular models. See Table 1 for comparison of models with Binney rotation curves. Figure 8 displays our fit for a prolate model with $\epsilon_p = \epsilon_\infty[1 - \exp(-r^3/\sigma_e^3)]$, where σ_e was varied for best fit. Where the line of sight intersects the disk more than once, the velocity displayed in the projected velocity field of Figure 8*b* is the intensity-weighted average of the velocity of each point intersected. The intensity shown in Figure 8*c* is the sum of the intensities at each point of the disk intersected by the line of sight. For the oblate model, the best fit was found for $\vartheta = 60° \pm 7°$, $\omega = 25° + 5°$, $r_z = 100''$, $r_m = 50''$ and $\sigma_s = 65''$. For the prolate model, $\vartheta = 60° \pm 7°$, $\omega = 25° \pm 5°$, $r_z = 90''$ and $120''$, $r_m = 53''$, and $\sigma_s = 80''$. For both models, $\chi = 35° \pm 5°$, $A = 290$ km s^{-1}, $c = 40''$, and $V_{sys} = 538$ km s^{-1} with respect to the local standard of rest (541 km s^{-1} heliocentric). Using equation (7.2), we found $\epsilon_p \Delta t = -1.2 \times 10^7$ yr and $\alpha_0 = 131\overset{\circ}{.}8$ for the oblate model with ϵ_p constant, and $\epsilon_\infty \Delta t = 2 \times 10^7$ yr and $\alpha_0 = -182°$ for the prolate model with $\epsilon_p = \epsilon_\infty[1 - \exp(-r^3/\sigma_e^3)]$ and $\sigma_e = 80''$. Since the infrared isophotes in the central region of the galaxy ($r < 60''$) are not significantly flattened, the ellipticity of the potential in this region must be very small. For an oblate model with $\epsilon_p = -0.01$ or axis ratio $q \approx 0.99$, $\Delta t = 1.2 \times 10^9$ yr. For a prolate model with $\epsilon_\infty = 0.2$, roughly equivalent to an axis ratio $1/q = b'/a' = 0.8$ as observed from the optical isophotes, we found $\Delta t = 1 \times 10^8$ yr. This time scale agrees with that estimated by Tubbs (1980). These models have a mass of $1.1 \times 10^{11}\ M_\odot$ inside 4.5 kpc which is the same as that of the circular models discussed in § 5 and that derived by van Gorkom et al. (1990).

We note that for a plane at an angle ω from the principal plane the contours of constant potential have ellipticity $\sim \epsilon_p \sin^2 \omega$, so that the orbits of the gas on this plane for both the oblate and prolate model with $\omega = 25°$ should be very nearly circular, so that our approximation of circular orbits is accurate for these models.

TABLE 1

Best-Fit Models with Binney Rotation Curves

Parameter	Geometry and Orbits: Planar, circular	Planar, noncircular	Warped, circular
V_{sys} (km s^{-1})[a]	540 ± 5	538 ± 5	538 ± 5
ϑ	$80° \pm 3°$	$80° \pm 3°$	$60° \pm 7°$
φ	...	$20° \pm 8°$	...
θ*	...	$-5°$	...
b/a	...	0.5	...
χ	$35° \pm 5°$	$37° \pm 5°$	$35° \pm 5°$
A (km s^{-1})	290 ± 20	300 ± 20	290 ± 20
c	$40'' \pm 15''$	$40'' \pm 15''$	$40'' \pm 15''$
σ_s	$65''$	$60''$	$80''$
σ_e	...	...	$80''$
α_0	...	...	$-182°$
$\epsilon_\infty \Delta t$ (yr)	...	...	2×10^7
ω	...	...	$25° \pm 5°$

[a] V_{LSR}.

7.4. *Discussion*

Since we obtained good fits using models whose constraints are taken from the Hα data, we conclude that the dynamics and geometry of the molecular material is identical to that of the ionized material seen in Hα. Specifically, our best-fit prolate model (Fig. 8) fits the data surprisingly well. There are some differences which can be mostly explained by pointing errors in the data. Differences may also be caused by non-axisymmetric variations in intensity on the disk such as might by caused by spiral arms. The parameters for this model were determined initially by fitting to the data obtained in 1989 March which consisted only of positions along the major and minor axes of the dust lane. The additional data obtained in 1991 June at the request of the referee fit remarkably well without adjustment of parameters; in fact, we were unable to improve the quality of the fit by adjusting the parameters. This gives confidence in the predictive power of the model. The best-fit oblate model (not displayed) fit the data well only in the inner regions (less than 60" from the nucleus). Use of a rotation curve without a core (eq. [5.2]) does not improve the fit to the data in the central regions. Models with lower α_0 fit better in the center than models with higher α_0, though they fit the data in the outer regions less well. By using a more accurate model for $\alpha(r)$, a model which fits the data better everywhere could be made. However, in order to do this, we would need to know better $\epsilon_p(r)$, the rotation curve, and the intensity as a function of radius. Even with models with lower α_0, there remain high-velocity tails in the data in the positions 0"–30" from the nucleus that were not present in the model profiles (these tails were also observed by Israel et al. 1990, 1991). As a result, there may be a dynamically independent system in the central region of Cen A. One possible explanation for this could be a circumnuclear disk (Israel et al. 1990, 1991), which would be responsible for the higher velocity wings of the central positions.

Steiman-Cameron & Durisen (1988) showed that the inclination $i(t)$ of a gas disk that is settling in a scale-free potential is given by

$$i(t) = i_0 \exp(-t/\tau_e)^3 , \tag{7.8}$$

where i_0 is the initial inclination, and τ_e is the settling time scale,

$$\tau_e = \left(\frac{v}{6}\right)^{-1/3} \left(\frac{\partial \dot{\alpha}}{\partial r}\right)^{-2/3} , \tag{7.9}$$

where v is the coefficient of kinematic viscosity $v = \alpha_v \sigma h$, $\dot{\alpha}$ is the precession rate (see eq. [7.1]) and $\alpha_v \approx f_a$ for clouds with low area filling factor f_a (Goldreich & Tremaine 1983). We note that in the inner regions ($r < 50''$), the potential is not scale free. However, the time scale for settling should be close to that of

FIG. 8*a*

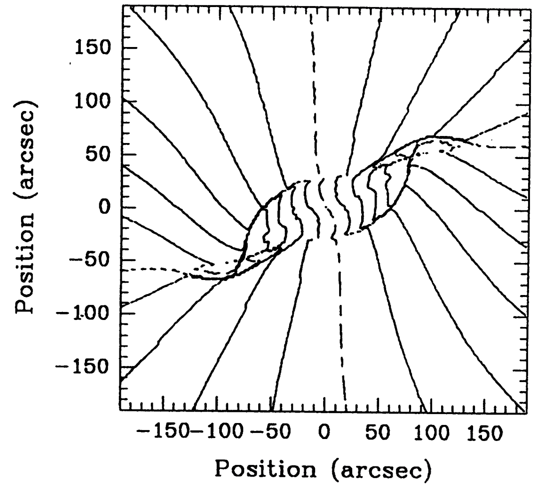

FIG. 8*b*

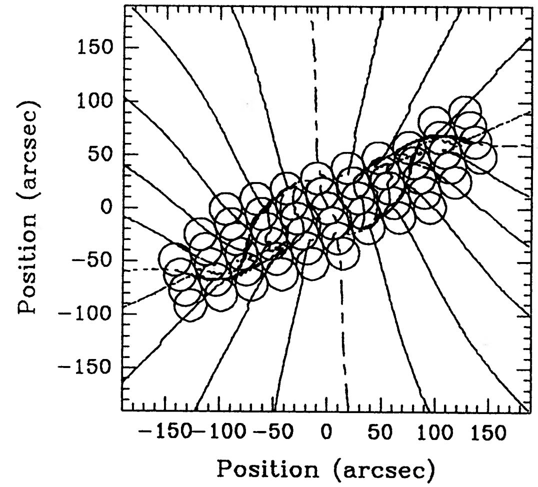

FIG. 8*c*

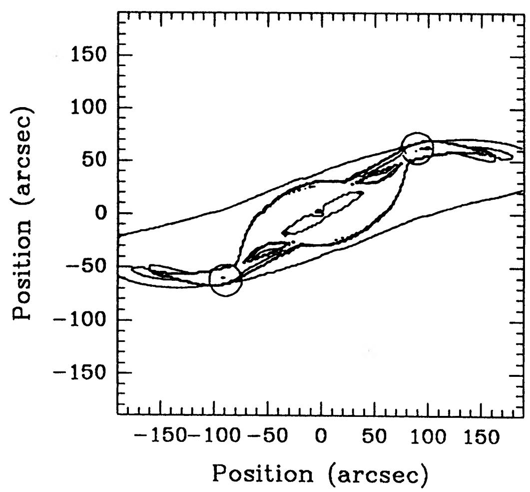

FIG. 8*d*

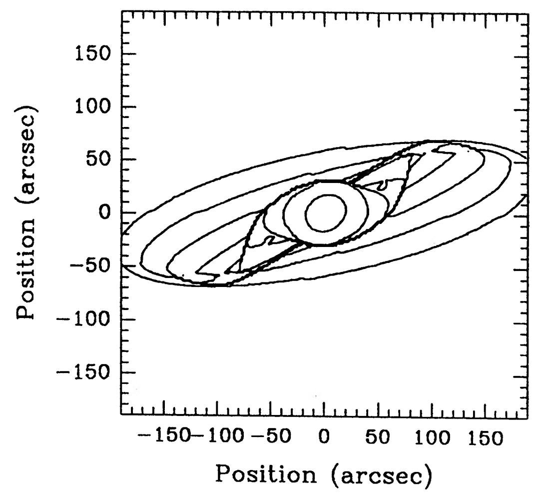

FIG. 8*e*

FIG. 8.—Inclined ring model for a prolate potential with ellipticity $\epsilon_p = \epsilon_\infty[1 - \exp(-r^3/\sigma_e^3)]$. (*a*) Profiles. (*b*) Projected model velocity field. Contours are 50 km s^{-1} apart. (*c*) Beam positions superposed on the projected velocity field. (*d*) Intensity contours. Contours are at 2%, 6%, 18%, and 26% of maximum intensity level (determined by J_{max}; see text for details). The small circles represent the approximate location of the peaks of the H I column density distribution (van Gorkom et al. 1990). (*e*) Projected orbits.

equation (7.9), and the inclination (eq. [7.8]) should settle exponentially though probably not to the third power of t. We estimated this time scale by taking the velocity dispersion $\sigma \approx 10$ km s^{-1} and $\alpha_v \approx 0.1$. For the oblate model with constant ellipticity $1.6 \times 10^9 < \tau_e < 4 \times 10^9$ yr for $r < 100''$, and for the prolate model $6 \times 10^8 < \tau_e < 1.2 \times 10^9$ yr over the same region where the shortest time scales for both models are at $r \approx 40''$. Since Δt is the same order of magnitude as τ_e for the oblate model with constant ϵ_p, a significant amount of settling should have occurred. We conclude that this model is inconsistent with the initial condition of gas on an inclined plane. For an oblate model with a lower ellipticity, and longer settling time scale (so that the disk would not have settled onto the principal plane of the potential), Δt would be larger than 10^9 yr, which seems rather long compared with the likely age of the merger. In order to consistently model the warp in an oblate potential, the inclination of the warp as a function of radius $\omega(r)$ would have to be modeled as well as $\alpha(r)$. However, $\Delta t < \tau_e$ for the prolate model, so this model is consistent with our initial hypothesis that the warp is the result of differential precession of gas that was initially on a plane with respect to the principal plane of the potential. We note that even though settling at this time scale may not have taken place, there may have still been a significant amount of inflow, which could have affected the shape of the warp. In addition we suspect that the rounding of the ellipticity of the potential in the central region of the galaxy may be a result of the gas disk falling into the center of the galaxy. The ellipticity of the central regions may not only be a function of radius but also of time. A more detailed model would have to take these factors into account.

In order to compare our prolate model with the large scale CO emission (Fig. 3), we made an integrated intensity map from our model (see Fig. 9). Note that the resemblance to Figure 3 is good, including an extension to the lowest contour level roughly 140″ on either side of the nucleus. We notice that the intensity of our model on the sky is primarily determined by the inclination of the surface of the warp, not by the surface density of the disk as a function of distance from the nucleus. Peaks in the emission can be located simply where there are folds in the disk. Figure 9 has peaks at $\approx 50''$ on either side of the nucleus. Similar features were also observed by Eckart et al. (1990b) in the CO(1–0) integrated intensity map. These features, which resemble the intensity contours of a molecular ring, may also be caused by the changing inclination of the warped molecular disk. The excess emission observed at the nucleus which is not present in the model is due to higher velocity wings which have been interpreted as evidence for a circumnuclear disk (Israel et al. 1990, 1991).

The overall shape of the intensity contours coincides both with the location of the optical dust lane and the H I emission.

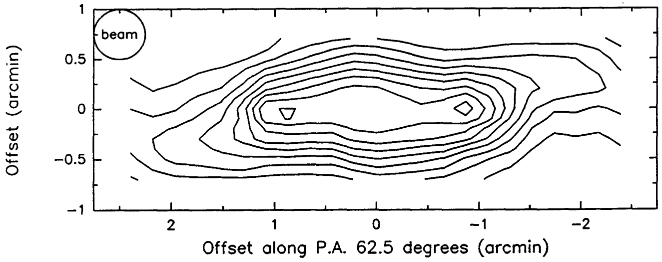

FIG. 9.—Integrated intensity contours for the prolate model of Fig. 8 for comparison with Fig. 3. Contours are at the same levels as in Fig. 3.

The two small circles in Figure 8c, at 109″ from the nucleus, indicate the locations of the peaks of the H I column density distribution (see Fig. 3 of van Gorkom et al. 1990), and they coincide nicely with the warp. The position angle of the H I emission on either side runs approximately east-west and so follows our intensity contours. We note that the overall shape of the model intensity distribution coincides with the optical dust lane as well. Because of its low filling factor, a significant fraction (dependent on the inclination of the disk) of the starlight behind the disk is visible. The optical appearance of the dust lane therefore depends on the transmission of the disk, as well as on its location in the galaxy. Figure 10 shows an overlay of this model on an optical image of Cen A (Graham 1979) we can see that portions of the disk at high inclination correspond to darker areas on the south side of the dust lane. Absorption seen on the north side cannot be due to gas described by this model. There is a fold in the disk at roughly 12″ to the south of the nucleus. This fold, which is nearer to us than the nucleus, is observable as a line of absorption in the near-infrared (J and H) (see Joy et al. 1991, Fig. 1). The Hα emission is brighter on the northern side of the dust lane (BTA) because there is less absorption on this side, rather than because the northern side is closer to us.

Finally, we note that although one of the three molecular absorption lines observed against SN 1986G by d'Odorico et al. (1989) correspond to the line-of-sight velocity of our modeled warp at the location of the supernova, the other two do not. As these authors discuss, it may be possible for a warped model, when extended out to radii beyond 300″, to match the velocities of these absorption lines. Since our CO data do not extend beyond 120″, our best-fitting model cannot be applied with any confidence at such large radii.

8. SUMMARY AND CONCLUSIONS

Using a rough estimate of the inclination of the disk ($\sim 80°$) derived from the best-fit circular models, we estimate the area filling factor of the molecular disk $0.03 < f_a < 0.12$ for $R < 60''$ and average cloud temperatures ≈ 10 K. We find that the thickness of the disk is less than 35 pc, and the velocity dispersion $\sigma < 10$ km s^{-1}. Using the Jeans stability limit for a disk undergoing star formation, we were able to extend these limits to the whole disk. Not only is the disk surprisingly thin and cold (meaning the clouds composing it have low velocity dispersion) but also the filling factor is so low that the molecular disk is optically thin everywhere except possibly at the points on the sky where the disk folds. Both of these conclusions are consistent with the observed Hα projected velocity field (BTA). We suspect that the Hα measurement of the velocity dispersion (BTA) is higher than our limit because of line blending caused by seeing more than one fold of the disk at each position on the sky. We note that they did observe line splitting in some areas. Eckart et al. (1990b) may have overestimated the velocity dispersion necessary to reproduce the CO(1–0) data for the same reason (see § 3).

In § 5 we found that circular orbits in a plane do not fit our data particularly well. Models of this kind are inconsistent with the observed position angles of the axes of the CO isophotes and the optical isophotes. In § 6 we discussed planar noncircular models (gas on the principal plane in a triaxial potential). With these models, we were not able to improve our fits to the data, though the alignment of the axes of the predicted and observed CO isophotes and the optical isophotes is somewhat improved by using these models. Allowing the ellip-

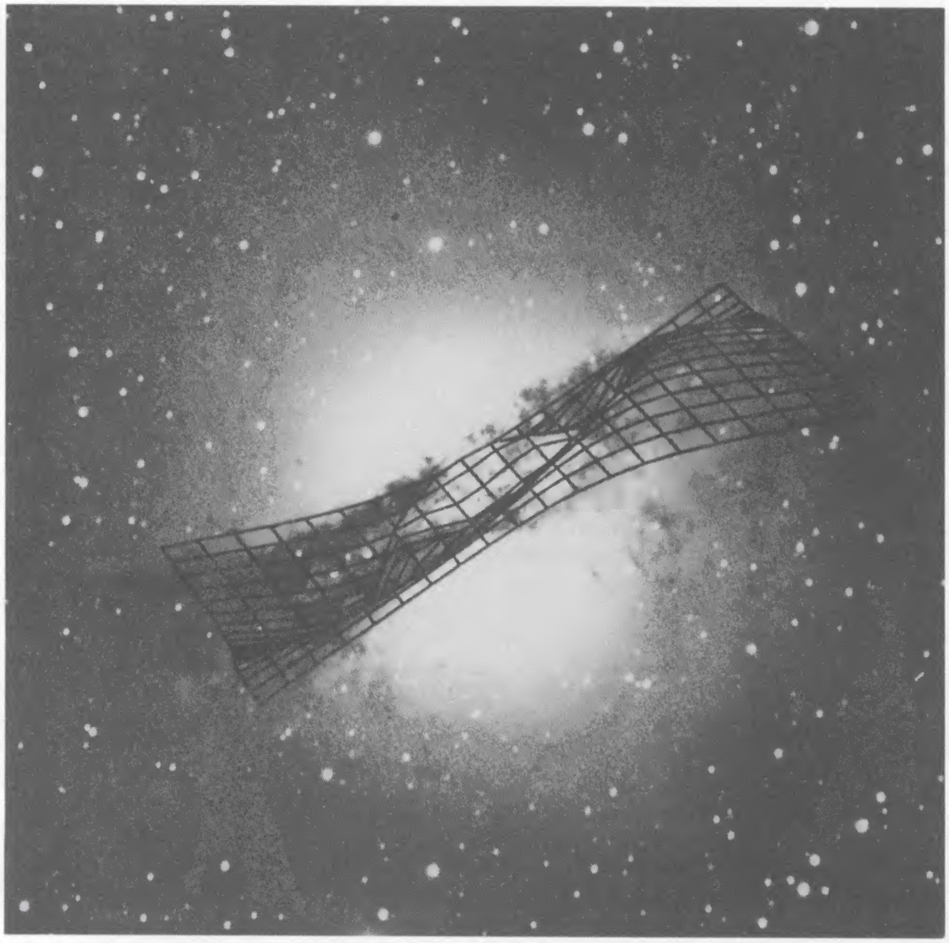

FIG. 10.—Overlay of the prolate model of Fig. 9 on an optical image of Cen A (Sandage 1961). The fold in the disk about 12″ south of the nucleus is observable as the line of absorption in the near-infrared (J and H) (see Joy et al. 1991, Fig. 1).

ticity of the potential to change as a function of distance from the nucleus does not improve the fits, although qualitatively such models have many of the same features that are observed in the Hα projected velocity field.

In § 7 we derived a simple model for a disk that has evolved from a planar system as a result of differential precession (Tubbs 1980). Using constraints derived from the Hα data we were able to find starting points for fitting. Because this was successful, we conclude that the ionized material seen in Hα is dynamically and geometrically identical to the molecular material observed in CO. Our best-fit model with an oblate potential is inconsistent with our initial assumptions (the gas should have settled onto the principal plane of the potential at the time scale needed in order to form the warp). In addition, the fit to the data for this model in the outer regions (more than 60″ from the nucleus) is not good. Our best-fit model with a prolate potential with ellipticity varying as a function of radius (Fig. 8) fits the data well and also shows agreement with the CO(2–1) integrated intensity contour map. Convolution of the intensity map of our model produces peaks in the integrated intensity contours that were observed by Eckart et al. (1990b) in CO(1–0). These features are not caused by a molecular ring or hole in the CO material in the center of the galaxy, but are caused by the changing inclination of the disk. The peak of the H I emission lands on the highest intensity contours of our warp model, and the intensity contours also follow the shape of the optical contours of the dust lane. Areas of the disk at high inclination correspond to darker areas of the dustlane as observed optically. There is a fold in the disk of our model roughly 12″ to the south that is coincident with the line of absorption in the near-infrared (J and H) observed by Joy et al. (1991). Wilkinson et al. (1986) found that an effectively stationary prolate model such as ours is consistent with their observation of the stellar velocity field of Cen A if the jet direction is not associated with an axis of symmetry of the galaxy. For this model, the inclination of the major axis of the potential is $60° \pm 7°$ with the gas at an angle of $25° \pm 5°$ above the equatorial plane of the potential, with the southern side nearest to us. This model would be tested further by comparison with a more spatially filled and more extended data set in CO(2–1), with higher resolution in CO(3–2) and by modeling the Hα data cube of BTA.

Since our warped model consists of clouds in circular orbits, it is not possible to obtain absorption lines at velocities other than the systemic velocity against the nuclear compact continuum source from the material in the warped disk. We note that it is possible that the gas disk is not only warped (not on a principal plane plane with respect to the potential), but that the potential is triaxial in which case the orbits of the gas could be significantly noncircular. In this case, one expects absorption lines against the nucleus at velocities that are either higher or lower than the systemic velocity, depending upon the direction of viewing. Because of numerous high-density molecular absorption lines and high-velocity wings in observed CO lines at the central positions in Cen A (Israel et al. 1991), it is more likely that there is a dynamically distinct system in the nucleus.

Gas warps, like the one we find in Cen A, may be responsible for much of the infrared emission from AGNs (Phinney 1989; Sanders et al. 1989). They may also provide a more dynamically plausible alternative to thick tori (Krolik & Begelman 1988) as a means of hiding the soft (but not the hard) X-ray emission (Koyama et al. 1989; Warwick et al. 1989) and the broad-line region of type II Seyfert and narrow-line radio galaxies. Morganti et al. (1990) have shown that the optical filaments of Cen A must be photoionized by a nuclear continuum source that is either hidden or highly anisotropic. These authors furthermore find that if this nuclear continuum is relativistically beamed, then Cen A may have beam power similar to that of BL Lac. Our best-fitting warp (consistent with both CO and infrared data) does not obscure the center of Cen A. Thus a torus or warped disk at radii much less than 20″ (300 pc) from the center seems required to obscure the active center of Cen A. There may also be gas outside the scale of our model ($r > 90''$) that obscures the nucleus.

The time scale estimated to create the warp is 10^8 yr. This time scale roughly agrees with that originally estimated by Tubbs (1980) for a transient warp. A more detailed model with a more accurate rotation and ellipticity curve which includes settling, inflow, and possible changing ellipticity as a function of time may somewhat alter the time scale. Since this time scale is shorter than the time scale from the initial galaxy-galaxy collision as estimated from the location of the thin stellar shells seen in the outer parts of the galaxy ([2×10^8]–[6×10^8] yr; Malin et al. 1983), we suggest that the process of the merger be modeled to estimate the time scale for a small galaxy to sink into the center of a larger elliptical and to see in detail the state of the dust after this occurs. Improvements in numerical methods and hydrodynamical codes in the past decade might make reexamination of these issues fruitful. We suspect that the impact parameter and angle of impact of the initial collision can be estimated from the stellar rotation that has been observed at larger radii (beyond 5′ from the nucleus) as determined from the radial velocities of planetary nebulae (Ford et al. 1989; Hui 1990), whereas the angular momentum vector and mass of the colliding spiral galaxy can be estimated from the molecular material in the center since no settling can have taken place on that time scale. With this knowledge, it should be possible to reconstruct the process of the merger.

It is a pleasure to thank Bharat Ratra and Ewine van Dishoeck for comments on the manuscript. We also acknowledge useful discussions with Robert Emmering, Connie Walker, Curt Cutler, and Garrett Biehle. We also acknowledge the anonymous referee whose detailed comments helped to improve the presentation of this paper. This research was supported in part by NSF grant AST 88-15132, NASA grants NAGW-2144 and NAGW-2142, and the Alfred P. Sloan Foundation (E. S. P.).

APPENDIX

MODIFIED HERNQUIST MODEL

Hernquist (1990) has introduced a simple spherical mass model with a projected surface density that closely resembles a de Vaucouleurs law and hence is useful for description of elliptical galaxies. Here we present a triaxial modification of this model, by defining its gravitational potential in spherical coordinates (r, θ, ϕ) as

$$V(r, \theta, \phi) = u(r) - v(r) Y_2^0(\theta, \phi) + w(r) Y_2^2(\theta, \phi) , \tag{A1}$$

with $Y_2^0 = 3/2 \cos^2 \theta - 1/2$ and $Y_2^2 = 3 \sin^2 \theta \cos 2\phi$ the usual spherical harmonics. We choose

$$u(r) = -\frac{GM}{r + r_0} , \qquad v(r) = -\frac{GMr_1 r}{(r + r_2)^3} , \qquad w(r) = -\frac{GMr_3 r}{(r + r_4)^3} , \tag{A2}$$

where $r_0, \ldots, r_4$ are constants, G is the gravitational constant, and M is the total mass of the model. The function $u(r)$ is the potential of the spherical Hernquist model.

The parameter r_0 is a density scale length, which can be related to the radius R_e which contains half of the projected surface density. In the spherical limit $R_e = 1.8153 r_0$. The remaining four parameters can be expressed in terms of the axis ratios of the density distribution at small and at large radii, where the surfaces of constant density are approximately ellipsoidal, i.e., $\rho \sim \rho(m^2)$ with $m^2 = x^2 + (y^2/p^2) + (z^2/q^2)$. The density falls off as $1/r^4$ at large radii and diverges as $1/r$ in the center.

At large radii, the modified Hernquist potential becomes Keplerian, and the closed orbits are nearly circular. At small radii, the potential becomes scale-free, and the orbits near the (x, y)-plane reach a limiting ellipticity ϵ given by

$$\epsilon = \frac{6(1 - p_0)}{1 + p_0 + 2q_0} \tag{A3}$$

where p_0 and q_0 are the central values of the axis scale lengths p and q.

REFERENCES

Baade, W., & Minkowski, R. 1954, ApJ, 119, 215
Begeman, K. 1987, Ph.D. thesis, Rijksuniversiteit, Groningen
Bertola, F., Bettoni, D., Danziger, I. J., Sadler, E. M., Sparke, L. S., & de Zeeuw, P. T. 1991, ApJ, 373, 369
Binney, J. J. 1981, MNRAS, 196, 455
Binney, J., & Tremaine, S. 1987, Galactic Dynamics (Princeton: Princeton University Press)
Bland, J., Taylor, K., & Atherton, P. D. 1987, MNRAS, 228, 595 (BTA)
Bosma, A. 1981, AJ, 86, 1791
d'Odorico, S., di Seregho Alighieri, S., Pettini, M., Magain, P., Nissen, P. E., & Panagia, N. 1989, A&A, 215, 21
de Zeeuw, P. T. 1990, in Dynamics and Interactions of Galaxies, ed. R. Wielen (Berlin: Springer), 263
de Zeeuw, P. T., & Franx, M. 1989, ApJ, 343, 617 (ZF)

Dufour, R. J., van den Bergh, S., Harvel, C. A., Martins, D. H., Schiffer, F. H., Talbot, R. J., Talent, D. L., & Wells, D. C. 1979, AJ, 84, 284
Eckart, A., Cameron, M., Genzel, R., Jackson, J. M., Rothermel, H., Stutzki, J., Rydbeck, G., & Wiklind, T. 1990a, ApJ, 365, 522
Eckart, A., Cameron, M., Rothermel, H., Wild, W., Zinnecker, H., Rydbeck, G., Olberg, M., & Wiklind, T. 1990b, ApJ, 363, 451
Ford, H. C., Ciardullo, R., Jacoby, G. H., & Hui, X. 1989, in IAU Symp. 131, Planetary Nebulae, ed. S. Torres-Peimbert (Dordrecht: Reidel), 335
Frogel, J., Quillen, A. C., & Graham, J. R. 1992, in preparation
Gardner, F. F., & Whiteoak, J. B. 1976, MNRAS, 175, 9P
Gerhard, O. E., & Vietri, M. 1986, MNRAS, 223, 377
Giles, A. B. 1986, MNRAS, 218, 615
Goldreich, P., & Tremaine, S. 1982, ARA&A, 20, 249
Graham, J. A. 1979, ApJ, 232, 60
Habe, A., & Ikeuchi, S. 1985, ApJ, 289, 540
———. 1988, ApJ, 326, 84
Harding, P., Jones, T. J., & Rodgers, A. W. 1981, ApJ, 251, 530
Haniff, C. A., Wilson, A. S., & Ward, M. J. 1988, ApJ, 334, 104
Hernquist, L. 1990, ApJ, 356, 359
Hernquist, L., & Quinn, P. J. 1988, ApJ, 331, 682
———. 1989, ApJ, 342, 1
Hui, X. 1990, talk presented at Aspen Workshop on Structure and Dynamics of Galaxies
Israel, F. P., van Dishoeck, E. F., Baas, F., de Graauw, Th., & Phillips, T. G. 1991, A&A, 245, L13
Israel, F. P., van Dishoeck, E. F., Baas, F., Koornneef, J., Black, J. H., & de Graauw, Th. 1990, A&A, 227, 342
Jog, J. C., & Solomon, P. M. 1984, ApJ, 276, 114
Joy, M., Harvey, P. M., Tollestrup, E. V., Sellgren, K., McGregor, P. J., & Hyland, A. R. 1991, ApJ, 366, 82
Joy, M., Lester, D. F., Harvey, P. M., & Ellis, H. B. 1988, ApJ, 326, 662
Kennicutt, R. C., Jr. 1989, ApJ, 344, 685
Koyama, K., Inoue, H., Tanaka, Y., Awaki, H., Tanako, S., Ohashi, T., & Matsuoka, M. 1989, PASJ, 41, 731
Krolik, J. H., & Begelman, M. C. 1988, ApJ, 329, 702
Lees, J. F. 1991, in Warped Disks and Inclined Rings around Galaxies, ed. S. Casertano, F. Briggs, & P. Sackett (New York: Cambridge Univ. Press), 50
Lees, J. F., & de Zeeuw, P. T. 1991, in preparation
Malin, D. F., Quinn, P. J., & Graham, J. A. 1983, ApJ, 272, L5
Marston, A. P., & Dickens, R. J. 1988, A&A, 193, 27
Morganti, R., Robinson, A., Fosbury, R. A. E., di Serego Alighieri, S., Tadhunter, C. N., & Malin, D. F. 1991, MNRAS, 249, 91
Nicholson, R. A., Bland-Hawthorne, J., & Taylor, K. 1992, 387, 503
Phillips, T. G., et al. 1987, ApJ, 322, L73
Phillips, T. G., Sanders, D. B., & Sargent, A. I. 1990, in Submillimetre Astronomy: Proc. of Kona Symposium, ed. G. D. Watt & A. S. Webster (Dordrecht: Kluwer), 223
Phinney, E. S. 1989, in Theory of Accretion Disks, ed. F. Meyer, W. J. Duschl, J. Frank, & E. Meyer-Hofmeister (Dordrecht: Kluwer), 457
Sandage, A. 1961, The Hubble Atlas of Galaxies (Washington: Carnegie Institution of Washington)
Sanders, D. B., Phinney, E. S., Neugebauer, G., Soifer, B. T., & Matthews, K. 1989, ApJ, 347, 29
Sansom, A. E., et al. 1987, MNRAS, 229, 15
Seaquist, E. R., & Bell, M. B. 1990, ApJ, 364, 94
Schwarz, U. J. 1985, A&A, 142, 273
Sparke, L. S. 1986, MNRAS, 219, 657
Stark, A. A. 1977, ApJ, 213, 368
Staveley-Smith, L., Bland, J., Axon, D. J., & Davies, R. D. 1990, ApJ, 364, 23
Steiman-Cameron, T. Y., & Durisen, R. H. 1988, ApJ, 325, 26
Tohline, J. E., Simonson, G. F., & Caldwell, N. 1982, ApJ, 252, 92
Tonry, J. L., & Schechter, P. L. 1990, AJ, 100, 1794
Tubbs, A. D. 1980, ApJ, 241, 969
Unger, S. W., Pedlar, A., Axon, D. J., Whittle, M., Meurs, E. J. A., & Ward, M. J. 1987, MNRAS, 228, 671
van Albada, T. S., Kotanyi, C. G., & Schwarzschild, M. 1982, MNRAS, 198, 303
van den Bergh, S. 1976, ApJ, 208, 673
van der Hulst, J. M., Golisch, W. F., & Haschick, A. D. 1983, ApJ, 264, L37
van Gorkom, J. H., van der Hulst, J. M., Haschick, A. D., & Tubbs, A. D. 1990, AJ, 99, 1781
Warwick, R. S., Koyama, K., Inoue, H., Tanako, S., Awaki, H., & Hoshi, R. 1989, PASJ, 41, 739
Wilkinson, A., Sharples, R. M., Fosbury, R. A. E., & Wallace, P. T. 1986, MNRAS, 218, 297